

RESEARCH

Open Access



^{13}C -MFA helps to identify metabolic bottlenecks for improving malic acid production in *Myceliophthora thermophila*

Junfeng Jiang¹, Defei Liu², Jingen Li², Chaoguang Tian², Yingping Zhuang¹ and Jianye Xia^{1,2*}

Abstract

Background *Myceliophthora thermophila* has been engineered as a significant cell factory for malic acid production, yet strategies to further enhance production remain unclear and lack rational guidance. ^{13}C -MFA (^{13}C metabolic flux analysis) offers a means to analyze cellular metabolic mechanisms and pinpoint critical nodes for improving product synthesis. Here, we employed ^{13}C -MFA to investigate the metabolic flux distribution of a high-malic acid-producing strain of *M. thermophila* and attempted to decipher the crucial bottlenecks in the metabolic pathways.

Results Compared with the wild-type strain, the high-Malic acid-producing strain *M. thermophila* JG207 exhibited greater glucose uptake and carbon dioxide evolution rates but lower oxygen uptake rates and biomass yields. Consistent with these phenotypes, the ^{13}C -MFA results showed that JG207 displayed elevated flux through the EMP pathway and downstream TCA cycle, along with reduced oxidative phosphorylation flux, thereby providing more precursors and NADH for malic acid synthesis. Furthermore, based on the ^{13}C -MFA results, we conducted oxygen-limited culture and nicotinamide nucleotide transhydrogenase (*NNT*) gene knockout experiments to increase the cytoplasmic NADH level, both of which were shown to be beneficial for malic acid accumulation.

Conclusions This work elucidates and validates the key node for achieving high malic acid production in *M. thermophila*. We propose effective fermentation strategies and genetic modifications for enhancing malic acid production. These findings offer valuable guidance for the rational design of future cell factories aimed at improving malic acid yields.

Keywords *Myceliophthora thermophila*, Malic acid, ^{13}C -MFA, Metabolomics, NADH

*Correspondence:

Jianye Xia

xiajy@tib.cas.cn

¹State Key Laboratory of Bioreactor Engineering, East China University of Science and Technology, Shanghai 200237, China

²Tianjin Institute of Industrial Biotechnology, Chinese Academy of Science, Tianjin 300308, China



© The Author(s) 2024. **Open Access** This article is licensed under a Creative Commons Attribution-NonCommercial-NoDerivatives 4.0 International License, which permits any non-commercial use, sharing, distribution and reproduction in any medium or format, as long as you give appropriate credit to the original author(s) and the source, provide a link to the Creative Commons licence, and indicate if you modified the licensed material. You do not have permission under this licence to share adapted material derived from this article or parts of it. The images or other third party material in this article are included in the article's Creative Commons licence, unless indicated otherwise in a credit line to the material. If material is not included in the article's Creative Commons licence and your intended use is not permitted by statutory regulation or exceeds the permitted use, you will need to obtain permission directly from the copyright holder. To view a copy of this licence, visit <http://creativecommons.org/licenses/by-nc-nd/4.0/>.

Background

Malic acid, a critical C4 dicarboxylic acid, is highly abundant in the food and beverage industry owing to its favorable taste and acidic properties [1]. In addition, as a significant C4 platform compound, it can be converted to a variety of chemicals that are beneficial for the textile, agricultural and medicine sectors.

Malic acid can be obtained through chemical synthesis, enzymatic transformation or microbial fermentation. As microbial fermentation results in lower costs and carbon emissions, microbial fermentation has been extensively investigated. Both naturally and via genetic engineering, bacteria, yeast and filamentous fungi have been reported to produce malic acid. Zhang et al. [2] utilized *Escherichia coli* as a platform to establish the strain XZ658 and achieved a malic acid content of 34 g/L after 3 days of fermentation. Zelle et al. [3] managed to produce 59 g/L malic acid, with a yield of 0.42 mol/mol glucose, in engineered *Saccharomyces cerevisiae* by overexpressing its innate pyruvate carboxylase and malate dehydrogenase and heterogeneously expressing the malate transporter from *Schizosaccharomyces pombe*. Additionally, a wide range of filamentous fungi, including *Aspergillus oryzae*, *Aspergillus niger*, and *Myceliophthora thermophila*, have been constructed to produce malic acid. Unlike other microorganisms, these fungi can directly utilize lignocellulose. Brown et al. [4] enhanced the rTCA flux of *A. oryzae* NRRL 3488, enabling malic acid production to reach 154 g/L after a fermentation period of 164 h. By amplifying the rTCA flux and deleting the oxaloacetate acetylhydrolase-encoding gene (*oahA*), Xu et al. [5] acquired a malic acid high-production strain with a fed-batch titer of 201.24 g/L. Li et al. [6] strengthened the rTCA, the malic acid transport system, and engineered a CO₂ absorption system in *M. thermophila*, reaching a final titer of 181 g/L, which was the highest level thus far for malic acid production with cellulose as the sole carbon source.

Although *M. thermophila* has demonstrated its ability to be engineered as a cell factory for malic acid, the mechanism underlying the production of malic acid by this nonmodel microorganism has not been thoroughly addressed. Systems biology has contributed significantly to the development of robust microbial cell factories. Integration and systematic analysis of the genome, transcriptome, proteome, metabolome, and metabolic fluxome allow us to decipher the cellular metabolic regulatory mechanisms, and bottlenecks can then be identified via numerical simulation [7, 8]. The metabolic flux distribution reflects the comprehensive cumulative effect of gene-protein-metabolite interactions under a specific condition of a strain [9]. Metabolic flux analysis (MFA) can aid in identifying the crucial nodes for product synthesis, enabling

metabolic engineers to optimize enzyme expression around these nodes, thus directing more metabolic flux to the product synthesis pathway. Over the past few decades, MFA has been applied to a variety of biological systems, ranging from simple systems such as *E. coli* [10] to complex eukaryotic microorganisms such as *S. cerevisiae* [11] to plant cells [12] and mammalian cells [13].

In this work, we employed ¹³C-MFA to compare the metabolic flux distribution between the high-production malic acid strain *M. thermophila* JG207 [6] and the wild-type (WT) *M. thermophila*. Furthermore, a targeted metabolomics study was also conducted. Energy and redox state analysis, together with metabolic flux distribution, were subsequently compared between the two strains to determine the potential key nodes involved in enhancing malic acid productivity. Finally, we validated the potential key nodes by checking the corresponding engineered strains. To the best of our knowledge, this is the first instance where ¹³C-MFA has been implemented in *M. thermophila* to decipher the bottleneck of metabolic production.

Results

Physiology of *M. thermophila* WT and JG207

As described in previous studies [6], malate transporter-encoding gene (*Aomae*), pyruvate carboxylase-encoding gene (*Aopyc*) from *A. oryzae* DSM1863 and hygromycin phosphotransferase encoding gene (*hph*) was inserted into pAN52-TB-Intron [14] to construct vector (pAN52-*P_{trpC}*-*hph*-*P_{tef}*-*Aomae*-*P_{AngpDA}*-*Aopyc*). The plasmid was linearized by *Bgl*II and introduced into *M. thermophila* ATCC 42,464 as described previously [15], generating strain JG207.

The two strains showed different physiological characteristics in batch culture (Fig. 1). And more detailed time-profile data of the fermentation process were placed in Additional file 1. Based on the measurements, various kinetic parameters were calculated (Table 1). The specific growth rate of JG207 did not significantly change compared to that of the WT strain while the glucose uptake rate of JG207 increased by approximately 36%. Consequently, the biomass yield of JG207 decreased by approximately 30%. The additional glucose taken up by JG207 was primarily utilized for the production of malic acid and a byproduct, succinic acid, with yields of 18.6% and 5.2% (Cmol/Cmol), respectively. Consistent with our results, previous studies reported that JG207 showed markedly higher expression levels of multiple sugar transporter genes with either glucose or cellulose as substrate compared with the WT [6]. Furthermore, the oxygen specific uptake rate (q_{O_2}) of JG207 was lower than that of the

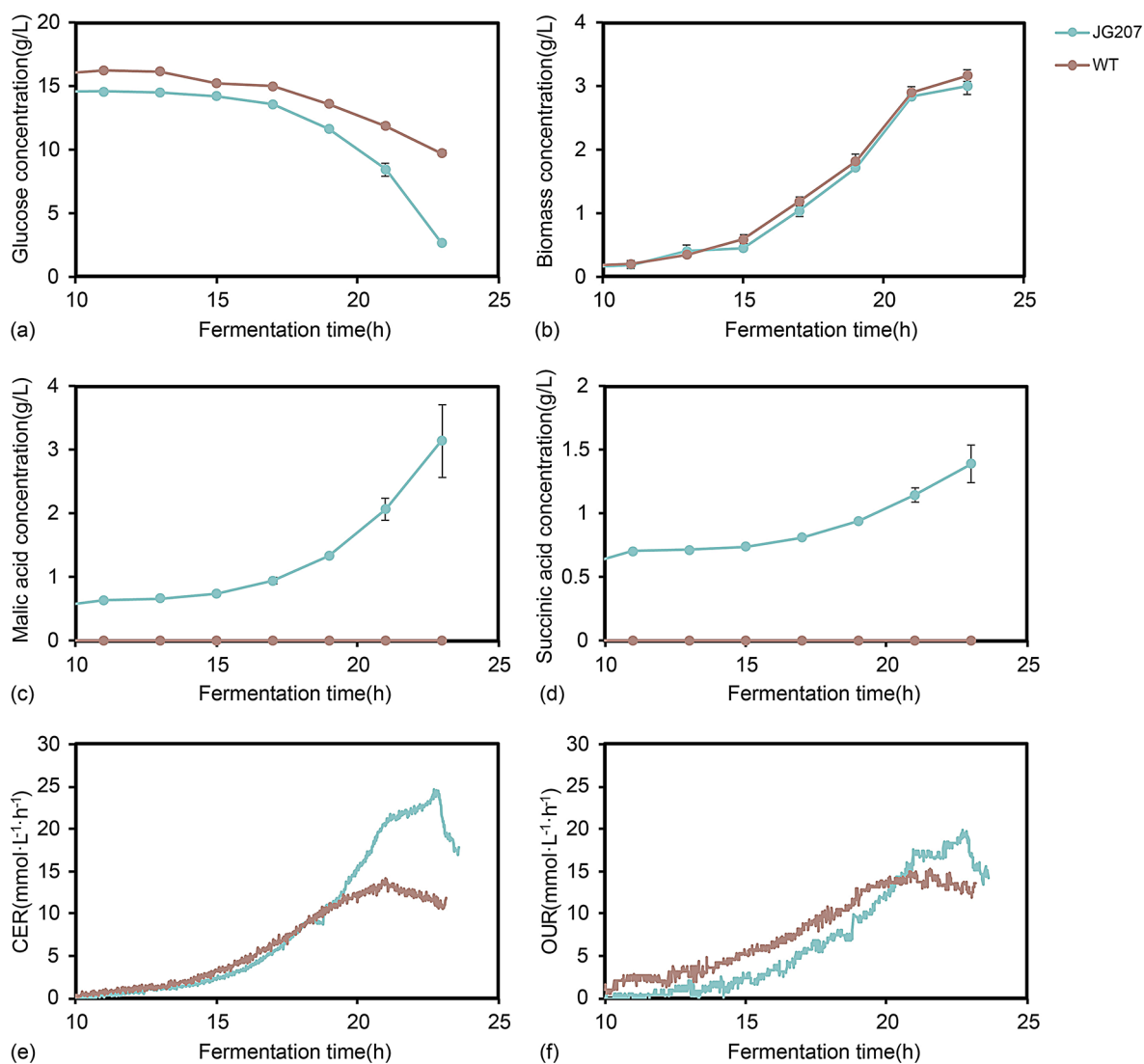


Fig. 1 Comparison of batch culture profiles between the *M. thermophila* wild-type (WT) strain and the high-production malic acid strain (JG207): (a) residual glucose concentration, values are means \pm SD (2 parallel reactors); (b) biomass concentration, values are means \pm SD (2 parallel reactors); (c) malic acid concentration, values are means \pm SD (2 parallel reactors); (d) succinic acid concentration, values are means \pm SD (2 parallel reactors); (e) carbon dioxide evolution rate (CER); (f) oxygen uptake rate (OUR)

WT strain while the carbon dioxide specific evolution rate (q_{CO_2}) of JG207 was greater.

Biomass synthesis reaction reconstruction

The biomass synthesis reaction is a crucial factor in determining the distribution of carbon flux and the utilization of precursors for growth. It plays a significant role in model validation and the calculation of metabolic fluxes [16, 17]. To enhance the reliability of the metabolic flux analysis results, we reconstructed the formula for the biomass synthesis reaction, which can be found in Additional file 5. To validate the accuracy of the biomass composition, we measured the content of each amino acid in the dry biomass (as shown in Table 2). The dry biomass of *M. thermophila*

WT strain was subjected to hydrolysis using 6 M HCl, and the resulting hydrolysate was analyzed using an amino acid analyzer. Among the amino acids detected, tryptophan was completely destroyed during the hydrolysis process, asparagine was hydrolyzed into aspartic acid, and glutamine was hydrolyzed to glutamic acid. Following the method of Ye et al. [17], in cases where amino acids were not distinguishable due to the hydrolysis process, we assumed an equal division of these undistinguished pairs of amino acids into two halves.

By determining the contribution of each amino acid to biomass synthesis, we aimed to improve the accuracy of the metabolic flux analysis results and ensure a

Table 1 Calculated kinetic parameters and carbon recovery in the exponential phase of *M. thermophila* WT and JG207, values are means \pm SD (2 parallel reactors)

	WT	JG207
Specific rate		
μ (h ⁻¹)	0.26 \pm 0.02	0.26 \pm 0.03
q_s (mmol/gDCW·h ⁻¹)	3.03 \pm 0.26	4.13 \pm 0.41
q_{mal} (mmol/gDCW·h ⁻¹)	Not detectable	1.15 \pm 0.31
q_{suc} (mmol/gDCW·h ⁻¹)	Not detectable	0.35 \pm 0.13
q_{CO_2} (mmol/gDCW·h ⁻¹)	5.21 \pm 0.17	6.16 \pm 0.03
q_{O_2} (mmol/gDCW·h ⁻¹)	6.6 \pm 0.2	5.69 \pm 0.03
Yield (Cmol/Cmol)		
$Y_{X/S}$	0.592 \pm 0.008	0.426 \pm 0.012
$Y_{mal/S}$	Not detectable	0.185 \pm 0.031
$Y_{suc/S}$	Not detectable	0.073 \pm 0.014
$Y_{CO_2/S}$	0.289 \pm 0.034	0.250 \pm 0.023

Table 2 Proteinogenic amino acid content measured in the dry biomass of *M. thermophila* WT strain (3 biological replicates)

Name	Value(mmol/gDCW)	SD
Ala	0.347	0.005
Ser	0.226	0.020
Asp	0.179*	0.017
Asn	0.179*	0.017
Thr	0.219	0.018
Gly	0.266	0.021
Glu	0.369*	0.013
Gln	0.369*	0.013
Val	0.179	0.014
Leu	0.332	0.033
Ile	0.168	0.012
Lys	0.270	0.026
His	0.061	0.006
Arg	0.226	0.015
Tyr	0.020	0.003
Phe	0.144	0.014
Cys	0.004	0.001
Met	0.008	0.000
Pro	0.194	0.018

*indicates undistinguishable pairs of amino acids)

more reliable representation of the carbon flux distribution in the system.

Differences in metabolic flux distribution revealed by 13 C-MFA and key enzyme activity measurements of central carbon metabolism pathways

To gain a deeper understanding of the metabolic differences between the two strains, we conducted ¹³C-MFA to estimate the intracellular flux distribution. Samples for ¹³C-MFA were taken every 10 min from 18 h after inoculation. The isotope information of amino acids (Additional file 2) confirmed that both strains' samples were in an isotopic steady state, satisfying the assumption for ¹³C-MFA [18]. The estimated central carbon metabolism

flux distributions of the two strains are shown in Fig. 2. Additional file 4 shows other unmapped reactions, including amino acid synthesis reactions. Additional file 3 lists the measured and simulated MDVs of amino acids. The flux confidence intervals are presented in Additional file 4, and χ^2 tests confirmed the statistical acceptability of the flux results.

The ¹³C-MFA best fit results (Fig. 2) showed distinct relative flux distributions at several key nodes between the two strains, such as G6P and PYR. Compared to the WT, strain JG207 exhibited a significant increase in the EMP (Embden–Meyerhof–Parnas) flux but exhibited a decrease in the PPP (pentose phosphate pathway) flux. Notably, the pyruvate carboxylation flux in JG207 was significantly enhanced, while the flux of pyruvate transported into the mitochondria remained largely unchanged. The surplus oxaloacetate was predominantly converted to malic acid via the reductive tricarboxylic acid cycle (rTCA) in the cytoplasm rather than being transported into the mitochondria. Therefore, the additional EMP flux in JG207 was directed toward pyruvate carboxylation for malic acid synthesis. Regarding the TCA pathway of JG207, the flux of the first reaction step did not differ significantly from that of the WT, but the downstream TCA reaction steps exhibited larger fluxes in JG207. The increased downstream TCA flux also led to increased CO₂ production, as indicated by the increased q_{CO_2} value.

Furthermore, we measured the enzyme activity of pyruvate carboxylase, which is the key node of genetic modification between JG207 and the WT. The enzyme assay samples were taken at the same time as those used for the ¹³C-MFA experiment (18 h after inoculation). The pyruvate carboxylase (PC) activity in JG207 was approximately 1.5 times greater than that in the WT (Fig. 3). Additionally, the results of ¹³C-MFA (Additional file 4) indicated that the optimal absolute fluxes of pyruvate carboxylation were 2.62 mmol/(g DCW·h) and 1.40 mmol/(g DCW·h) for JG207 and WT, respectively, confirming the increased pyruvate carboxylation flux in JG207.

Overall, the combination of 13 C-MFA and enzyme activity measurements provided valuable insights into the metabolic differences between the two strains, highlighting key nodes and flux alterations that contributed to the observed changes in malic acid production.

Comparison of intracellular NADH flux and its effects on malic acid synthesis

To investigate the effect of cofactors on malic acid synthesis, we analyzed the intracellular NADH flux, encompassing both its production and consumption fluxes (Fig. 4). Consistent with the higher substrate uptake rate, the absolute flux related to NADH in JG207 was greater than that in the WT strain. For both strains, the EMP

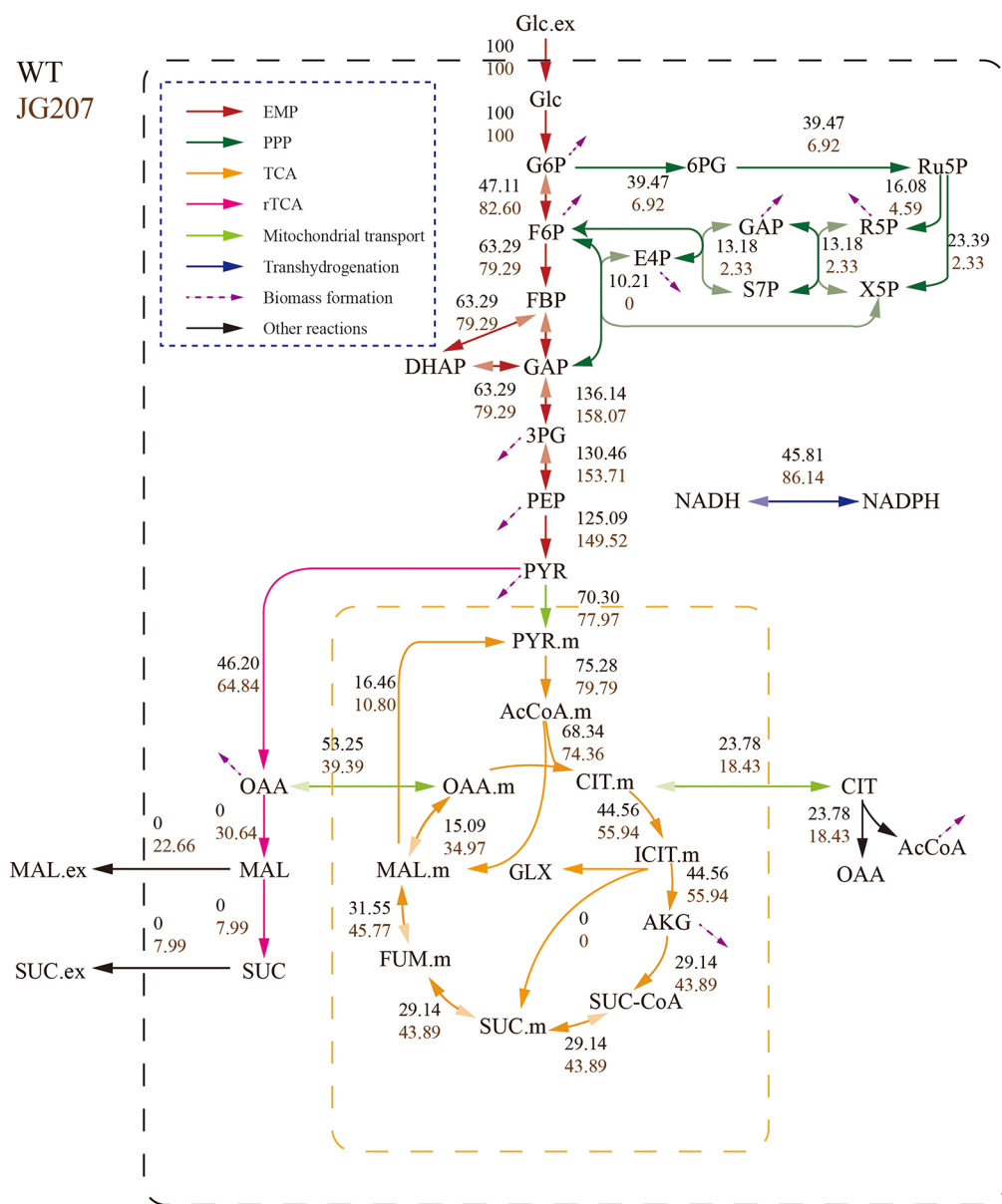


Fig. 2 Relative flux distribution (ratio to glucose uptake flux) of the WT (upper number in black) and JG207 (lower number in brown). A reaction with two side arrows indicates a reversible reaction, with the side with a dark arrow indicating the net flux direction

and the TCA pathways served as the primary pathways for NADH production. Under the experimental conditions, approximately 60% of the total NADH production originated from the TCA cycle. The major consumption (more than 80%) of intracellular NADH occurs in the mitochondria, where oxidative phosphorylation generates ATP to provide energy and transhydrogenation occurs to balance the cofactor. The NADH produced by the TCA cycle is insufficient for mitochondrial consumption, and NADH in the cytoplasm needs to be shuttled into the mitochondria for replenishment. Additionally, NADH was also consumed in the cytoplasm for rTCA reactions. Thus, there is competition for cytosolic NADH

in the JG207 strain. The reduced consumption of NADH by oxidative phosphorylation in JG207 reduces the requirement for cytosolic NADH shuttling, which facilitated the accumulation of NADH in the cytoplasm.

Furthermore, we observed increased transhydrogenation flux (from NADH to NADPH) in JG207. This increased flux is unfavorable for the accumulation of NADH in the cytoplasm. However, due to the greater EMP flux and decreased PPP flux in JG207, along with the relatively unchanged demand for NADPH at the same specific growth rate, a greater transhydrogenation flux is necessary to meet the NADPH requirements for cell growth.

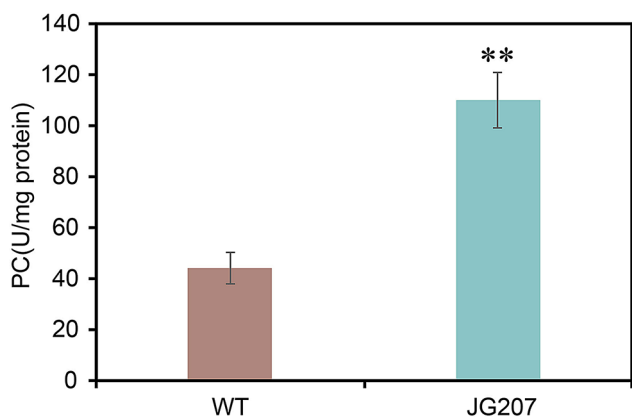


Fig. 3 Enzyme activities of PC (pyruvate carboxylase) for WT and JG207 in the mid-exponential phase (18 h after inoculation), values are means \pm SD (3 biological replicates). One unit was defined as the consumption of 1 nmol of NADH per min (** indicates that there was a very significant difference with a p value < 0.01)

Intracellular metabolite pool analysis between the two strains

We conducted an extensive analysis of intracellular metabolite pools in the two strains using LC-MS and a

Coenzyme Assay Kit (Solarbio). The resulting heatmap (Fig. 5) showed a distinct profile for JG207, characterized by upregulated metabolites such as MAL, FUM, SUC, and cofactors. This observation primarily stems from increased pyruvate carboxylation flux and enhanced flux through the rTCA, leading to the accumulation of these metabolites within the pathway. Notably, there was a significant increase in the NADH/NAD⁺ ratio in JG207, whereas there was no significant difference in the NADPH/NADP⁺ ratio (Fig. 6). To a certain extent, this can explain the higher hydrogen transfer flux of JG207. And this shift toward a lower energy state (lower ATP pool) was attributed to a reduction in oxidative phosphorylation flux, resulting in decreased NADH consumption and ATP synthesis.

Furthermore, alterations in the amino acid pool size were observed, correlating with the availability of precursor molecules for synthesis. For instance, the decreased pool of pyruvate-derived amino acids in JG207 may be attributed to an increased pyruvate carboxylation flux, leading to diminished synthesis of corresponding amino acids. Similarly, the reduced pool of oxaloacetate-derived amino acids can be attributed

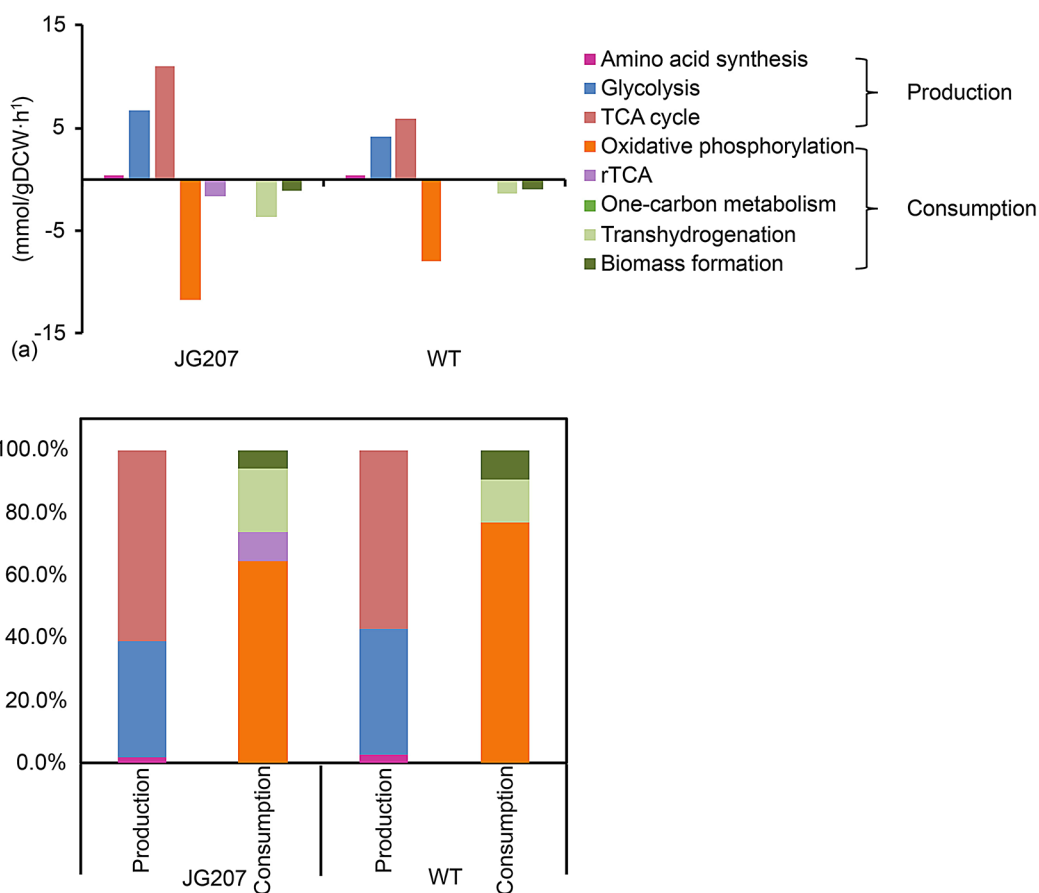


Fig. 4 The balance for NADH production and consumption in JG207 and WT: (a) absolute net flux of NADH (positive means production and negative means consumption); (b) the percentage of NADH produced or consumed by each pathway

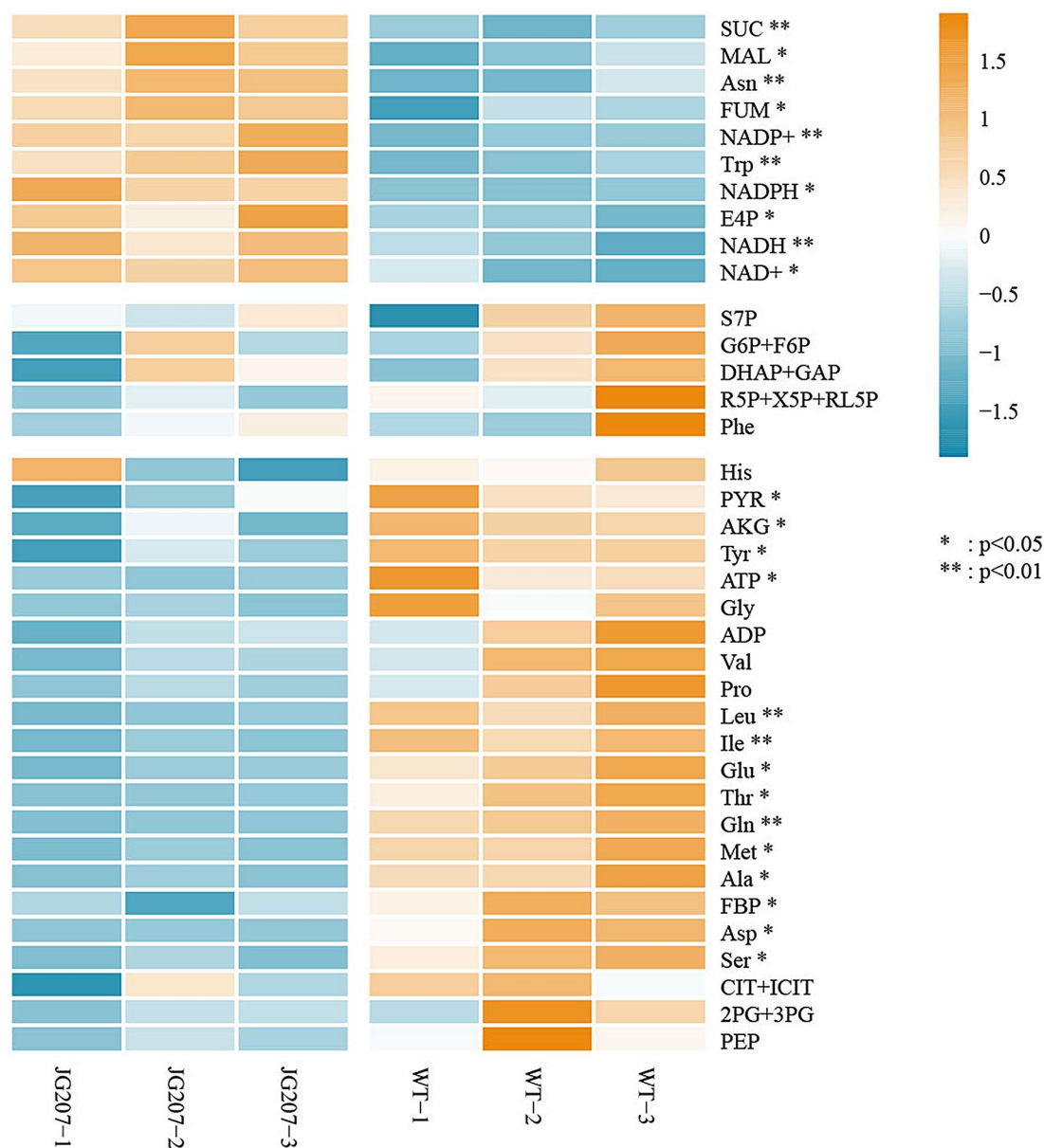


Fig. 5 Heatmap of metabolite levels in the WT and JG207 strains (3 biological replicates, orange indicates higher concentrations, and blue indicates lower concentrations)

to the redirection of oxaloacetate toward malic acid and succinic acid production. Additionally, the diminished pool of α -ketoglutarate-derived amino acids in JG207 can be linked to enhanced decarboxylation flux of α -ketoglutarate.

Overall, these findings shed light on the intricate metabolic changes occurring in engineered strains, providing valuable insights into pathway dynamics and potential targets for further optimization.

Validation of key regulatory nodes found by ^{13}C -MFA

Through ^{13}C -MFA study, it was found that the key to a high yield of malic acid is a sufficient supply of NADH in

the cytoplasm, supporting high rTCA flux for high malic acid accumulation. However, the high level of cytoplasmic NADH in JG207 also leads to the high expression of transhydrogenase, which consumes NADH to NADPH and leads to insufficient NADH to support a high malic acid yield. Therefore, knocking out the gene encoding the transhydrogenase may fundamentally solve this problem. On the other hand, inhibiting the electron transport chain can promote the accumulation of NADH in the cytoplasm. To verify this hypothesis, transhydrogenase gene knockout and oxygen limitation experiments were performed.

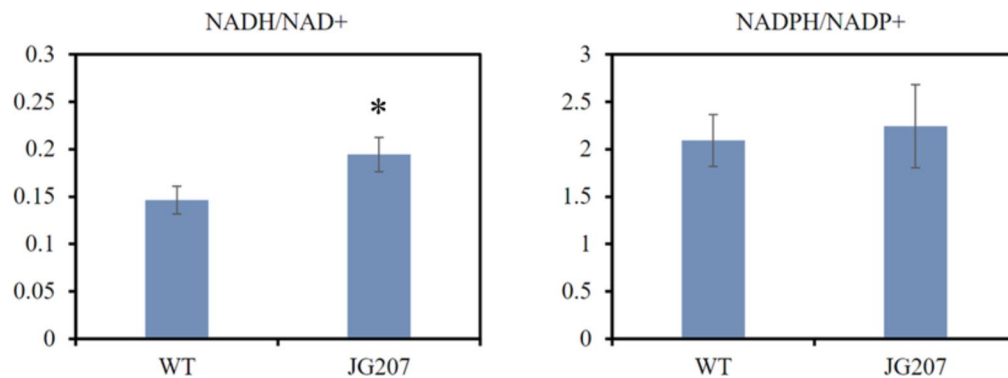


Fig. 6 The ratios of NADH/NAD⁺ and NADPH/NADP⁺ in the two strains (* indicates that there was a significant difference with a p value < 0.05), values are means ± SD (3 biological replicates)

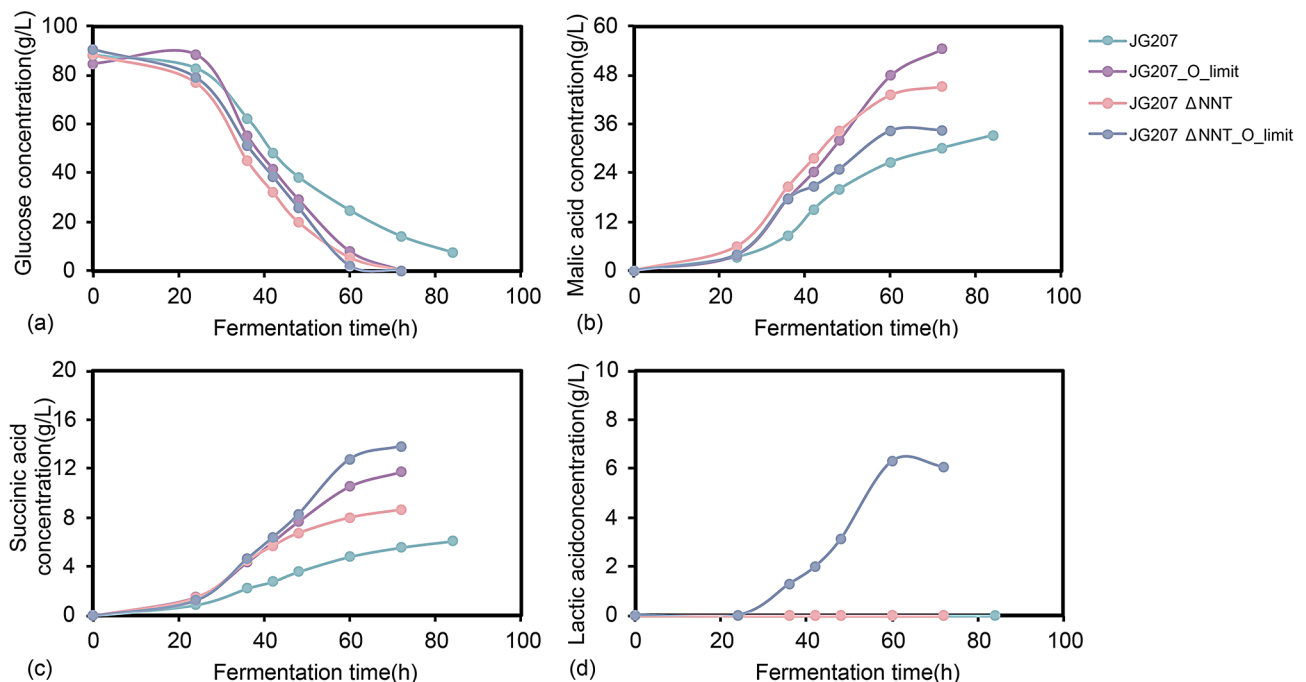


Fig. 7 Comparison of extracellular metabolite profiles during batch culture of *M. thermophila* JG207 and JG207ΔNNT with or without oxygen limitation: (a) residual glucose concentration; (b) malic acid concentration; (c) succinic acid concentration; (d) lactic acid concentration

We knocked out the nicotinamide nucleotide transhydrogenase (*NNT*) gene in the JG207 strain and evaluated organic acid production under several oxygen supply levels (Fig. 7). The results revealed that both oxygen-limited culture and *NNT* gene knockout promoted malic acid synthesis, and the yields (Cmol/Cmol) at 72 h of fermentation increased from 36.9 to 57.6% and 45.8% respectively (Additional file 7). However, succinic acid production also increased under these conditions. Additionally, the *NNT* knockout strain did not improve malate yield under oxygen-limiting conditions. Under this condition, the yield of the byproduct succinate was the highest, and a new byproduct lactate was generated, which may be attributed to excess NADH accumulation under oxygen-limiting conditions. In the context of malic acid

fermentation, our experiment confirmed the key role of NADH as a cofactor.

Discussion

Metabolic changes and mechanisms about malic acid synthesis

Microorganism cells exhibit both metabolic flexibility [19] and robustness [20] when the external environment or its genotype changes. In this study, alterations in metabolic flux distribution underscored the adaptability of metabolic networks in *M. thermophila*. Notably, significant differences were observed at the G6P node between the JG207 and WT strains. Consistent with previous findings of Heyland et al. [21], a correlation between biomass yield and pentose phosphate pathway

flux was evident, with the WT exhibiting a greater biomass yield associated with high PP pathway flux. This phenomenon can be attributed, in part, to the inhibitory effect of ATP on glucose-6-phosphate isomerase [22], as evidenced by the greater intracellular ATP concentration in the WT strain than in the JG207 strain. Consequently, the relatively higher PPP flux in the WT can be attributed to ATP-mediated inhibition of glucose-6-phosphate isomerase. It should be noted that the PP pathway flux is usually linked to the cell growth rate, corresponding to a sufficient supply of NADPH [23]. As the specific growth rates of the two strains were similar, the requirement for NADPH should not significantly differ. Thus, the lower flux of the PP pathway in JG207 resulted in greater transhydrogenation flux (from NADH to NADPH) to supply enough NADPH in this strain.

Furthermore, the flux distribution in the TCA cycle pathway revealed subtle differences between JG207 and the WT. While the initial step catalyzed by pyruvate dehydrogenase showed no difference, subsequent steps displayed gradually increasing fluxes in JG207. This can be attributed to the alleviation of isocitrate dehydrogenase inhibition [24] due to the lower AKG pool in JG207. Consequently, subsequent TCA reactions in JG207 exhibited greater relative fluxes, resulting in increased NADH production to compensate for the greater consumption. In addition, the increased flux in mitochondrial oxaloacetate regeneration within JG207 cells resulted in decreased transport of cytosolic oxaloacetate to the mitochondria, favoring the redirection toward the rTCA.

In summary, the metabolic fluxes of JG207 are reconfigured to favor malic acid synthesis. Enhanced glycolysis provides more pyruvate and NADH in the cytoplasm, while increased downstream TCA flux and reduced oxidative phosphorylation result in the accumulation of NADH in the mitochondria. This results in decreased NADH shuttle flux and provides more NADH for rTCA in the cytoplasm, which favors the accumulation of malic acid.

Strategies for further accumulation of malic acid

In addition to direct genetic modification, cofactor engineering is an effective way to increase the yield of target products [25]. The synthesis of cofactor-dependent products could be promoted by accumulating related cofactors. The methods of accumulating cofactors include promoting their production or reducing their consumption. For instance, Qi et al. [26] achieved a significant increase in the NADPH pool size by 4.4-fold through the inactivation of glucose-6-phosphate isomerase and the overexpression of glucose-6-phosphate dehydrogenase in isobutanol-producing *Bacillus subtilis*, resulting in notable improvements in isobutanol production and yield. Similarly, Wu et al. [27] increased the NADH pool size

by knocking out the NADH dehydrogenase genes (*nuoC/nuoD*) and reduced NADH consumption by knocking out lactate dehydrogenase (*ldh*), resulting in substantial enhancements in 2,3-butanediol production. Maximilian R et al. [26] reported that deleting the external NADH dehydrogenase (NDE1) coupled to the respiratory chain had a positive impact on 1,2-propanediol, which needs NADH. Ho et al. [27] reported that when *NNT* was knocked out, the NADH content increased, the flux of TCA decreased, and the flux of reductive carboxylation increased under new steady-state metabolic conditions. Nicotinamide nucleotide transhydrogenase (*NNT*) is located in the inner membrane of mitochondria and the transhydrogenation reaction catalyzed by *NNT* is reversible [28]. We obtained the accurate direction of the transhydrogenation reaction (NADH to NADPH) through ¹³C-MFA. Subsequently, the production of malic acid was increased by knocking out *NNT*. Although high titers of malate were achieved in the engineered strains, the accumulation of succinate, the main byproduct, during the fermentation process limited further increases in malate production. In *Escherichia coli*, the deletion of fumarase genes (*frdB* and *frdC*) reduced succinate production and increased malate production [2]. However, this strategy did not work for malate-producing filamentous fungi. In a recent study, Gu et al. [29] eliminated the byproduct succinate by deleting the mitochondrial carriers of pyruvate and malate, overexpressing *Mtsfc* (encoding the mitochondrial C4-dicarboxylate acid carrier) to import the cytosolic succinate into mitochondria, and designing a succinate uptake system. In addition, our study showed that byproduct lactic acid was produced under oxygen-limited conditions after knocking out the *NNT* gene. Excess NADH causes pyruvate to directly generate lactate instead of participating in the rTCA pathway. This seems to require an appropriate NADH level to maximize the flux of rTCA. It is difficult to achieve for metabolic engineering, but it is very useful for optimizing fermentation processes. Fermentation with different dissolved oxygen levels will be used to explore the appropriate NADH level and increase malic acid production.

Conclusions

In this study, we investigated the metabolic pathway of malic acid synthesis in *M. thermophila* by employing a combination of ¹³C-MFA and isotope-based targeted metabolomics. We found that the availability of cytosolic NADH plays a crucial role in malic acid synthesis. Specifically, in strain JG207, a greater flux through the EMP pathway provided both precursors and NADH for malic acid production. At the same time, increased flux through the downstream TCA cycle coupled with reduced oxidative phosphorylation reduces the requirement for cytosolic NADH shuttling, which is beneficial for malic acid

synthesis. In addition, higher transhydrogenation flux was observed in JG207. Drawing from these insights, we proposed effective fermentation strategies and genetic modifications to enhance malic acid production. These findings offer valuable guidance for the rational design of future cell factories aimed at improving malic acid yields.

Methods

Strains and culture conditions

Two *M. thermophila* strains were obtained from the *Key Laboratory of Systems Microbial Biotechnology, Tianjin Institute of Industrial Biotechnology, Chinese Academy of Sciences*. *M. thermophila* JG207 expressed the malic acid transporter gene (*Aomae*) and pyruvate carboxylase gene (*Aopyc*) from *A. oryzae* DSM1863, compared with *M. thermophila* WT. The two strains were subsequently grown on Vogel's minimal medium supplemented with 2% glucose at 35 °C for 14 days to obtain mature conidia.

Fermentation of the two strains was performed in 500 mL reactors (T&J Bio-engineering Co. LTD, Shanghai, China) with 300 mL of medium at 45 °C, and each reactor was inoculated with 10⁶ spores per 1 mL of medium. Agitation and aeration were maintained at 300 rpm and 0.5 L/min, respectively, during early fermentation. After the spores germinated and entered the exponential phase, the agitation increased to 500 rpm. The fermentation medium (per liter) contained 15 g of glucose, 1.5 g of (NH₄)₂SO₄, 0.15 g of KH₂PO₄, 0.15 g of K₂HPO₄, 0.1 g of MgSO₄·7H₂O, 0.1 g of CaCl₂·2H₂O, 1 mL of biotin (0.1 g/L), 1 mL of trace element solution (Vogel salts), and 30 g of CaCO₃. The CaCO₃ maintained a pH of approximately 6 during the whole batch fermentation.

Fermentation to verify production was performed in 2 L reactors (Dasgip) with 1.2 L medium. The fermentation medium (per liter) contained 80 g of glucose, 8 g of peptone, 0.15 g of KH₂PO₄, 0.15 g of K₂HPO₄, 0.1 g of MgSO₄·7H₂O, 0.1 g of CaCl₂·2H₂O, 1 mL of biotin (0.1 g/L), 1 mL of trace element solution (Vogel salts), and 80 g of CaCO₃. For the 4 groups of experiments, the same control strategy was used during the exponential growth phase, which continued until 24 h after inoculation. Aeration and pressure were set to 1 L/min and 0.2 Mpa, respectively. The initial agitation was set to 400 rpm, and the agitation was increased during the period to ensure that the DO is not less than 40%. After the exponential growth phase, the oxygen-limited experimental group maintained DO at 0 by reducing the agitation.

¹³C labeling experiments

In the ¹³C labeling experiments, the glucose used in the fermentation medium was replaced with labeled glucose. It has been reported that proper combinations of different ¹³C-labeled tracers have a large impact on the accuracy of estimated fluxes for different pathways [30, 31].

Therefore, the tracers used in this experiment contained 50% ¹²C-Glucose, 30% [U-¹³C]-Glucose and 20% [1-¹³C]-Glucose (isotopic enrichment 98–99%, Cambridge Isotope Laboratories, Inc.) to obtain more estimates of metabolic fluxes.

Samples for ¹³C-MFA were taken from cells at the mid-exponential phase (from 18 h after inoculation). At this time, the specific growth rate reaches the maximum value and remains constant, at which point metabolism is in a steady state [16]. The quenching solution and extraction method refer to *P. chrysogenum* and *A. niger* [32–34]. Since the beginning of sampling, 2 mL of broth was rapidly added to 10 mL of precooled quenching solution (−30 °C, 40% v/v methanol solution) every 10 min until 6 samples were taken. Vacuum filtration was used to separate the filter cake, and precooled quenching solution was used to wash the filter cake. The washed filter cake was added to prewarmed 25 mL of ethanol solution (75% v/v) and extracted for 3 min at 95 °C. The supernatant was collected by vacuum filtration and concentrated by a vacuum centrifugal concentrator. The MDVs (mass distribution vectors) of amino acids were determined via UPLC-MS/MS (SCIEX QTRAP 6500). And ion pair information of amino acids containing ¹³C isotopes were shown in Additional file 3.

Determination of extracellular metabolites

The specific growth rate was calculated from the dry cell weight. Three milliliters of broth was added to 5 mL of 1 mol/L HCl to dissolve excess CaCO₃. Biomass was collected by vacuum filtration. The filter paper was dried for 1 min with microwave oven, and the weight was recorded before filtration. Then, the wet filter with biomass was placed in a microwave oven and allowed to dry for 5 min, after which the weight was recorded.

The extracellular glucose and organic acid contents were determined by high-performance liquid chromatography (HPLC; e2695; Waters, Manchester, United Kingdom). Before detection, the broth taken from the bioreactor needs to be preprocessed. Then, 1 mL of 2 M H₂SO₄ was added to 1 mL of broth, and the mixture was incubated at 80 °C for 30 min and vortexed at intervals. Then, 2 mL of distilled water was added and mixed, and obtained the supernatant by filtration. The glucose and organic acid concentrations were determined with a Waters 2414 refractive index detector and an Aminex HPX-87 H column (Bio-Rad). H₂SO₄ (5 mM) was used as the mobile phase with a constant flow rate of 0.6 mL/min at 50 °C.

Enzyme assay

Samples for the enzyme assay were taken in the mid-exponential phase (18 h after inoculation). Then, 50 mL of medium was poured into a Büchner funnel containing

four layers of gauze. The mycelia were washed with distilled water until most of the CaCO_3 was removed and then collected. Protein was extracted from disrupted mycelial cells using a freezing grinder (Jing Xin, Shanghai, China) at -20°C . The total protein content was quantified by the Bradford method. PC activity was measured with a pyruvate carboxylase (PC) Assay Kit (Solarbio).

Analysis of intracellular metabolite concentrations

Isotope dilution mass spectrometry [35] is mainly used to eliminate the ion suppression effect caused by electrospray ionization in mass spectrometry measurements. The ^{13}C isotope-labeled internal standard required for the experiment was obtained by culturing *P. pastoris* with $\text{U-}^{13}\text{C}$ glucose as the sole carbon source. Samples for metabolome analysis were taken from cells at the mid-exponential phase (18 h after inoculation). The sampling process was similar to that used for the ^{13}C labeling experiments, except the ^{13}C internal standard solution was added to the prewarmed extractant during the extraction. The metabolite pools were determined with UPLC-MS/MS (SCIEX TRIPLETOF 6600).

A Coenzyme Assay Kit (Solarbio) was used for analysis of the levels of NADH, NAD^+ , NADPH and NADP^+ . Approximately 1 mL of broth was extracted to collect the coenzymes. The remaining processes were described in the introduction (Solarbio).

Determination of biomass amino acid composition

The methods for determining the biomass amino acid composition were modified from Carnicer et al. [36]. Approximately 3 mg of lyophilized biomass was hydrolyzed with 5 mL of 6 M HCl at 110°C for 24 h. Before hydrolysis, N_2 was used to remove O_2 from the tube. The hydrolysate was concentrated in vacuo to a constant weight, and 1 mL of 0.02 M HCl was added to dilute the samples. The supernatant was collected by filtration through a $0.22\ \mu\text{m}$ membrane. Twenty microlitres of supernatant was used for amino acid analysis.

LC-MS analysis

The metabolic samples were separated on a zic-HILIC column ($100\ \text{mm} \times 2.1\ \text{mm}$, $3.5\ \mu\text{m}$) (Merck, German). Solvents were composed of water/acetonitrile/ammonium acetate (A: 100%/0%/10 mM, B: 0%/100%/0 mM). The LC methods were 0–3 min (90% B), 3–25 min (90–60% B), 25–30 min (60% B), and 30–38 min (90% B). A flow rate of 0.3 mL/min was employed.

Calculation of metabolic fluxes

The metabolic fluxes were calculated by INCA [37], which is based on the EMU framework [38]. The model used in the calculation was constructed according to a genome-scale metabolic model for *Myceliophthora*

thermophila [39]. The difference between the simulated and measured values of MDV and the extracellular rate was minimized via least-squares regression to calculate metabolic flux. A χ^2 -statistical test was performed to determine the goodness-of-fit [40].

Construction of *M. thermophila* JG207 ΔNNT

For the deletion of *NNT* (Mycth_2125469) via the CRISPR/Cas9 system, a guide RNA (gRNA) expression cassette was constructed as described previously [41]. Briefly, a specific sgRNA target site in *NNT* was identified using the sgRNACas9 tool [42]. The oligo with low off-target probability was selected (Additional file 8). The *M. thermophila* U6 promoter and a target-directed sgRNA fragment were amplified from the U6p-sgRNA plasmid [41], assembled by overlapping PCR and cloned into a pJET1.2/blunt cloning vector, forming the plasmid U6-NNT-sgRNA. The vectors carrying the donor DNA sequence of *NNT* were constructed. The 5' and 3' flanking fragments of *NNT* amplified from the *M. thermophila* genome and the selection marker cassette P_{trpC}-neo were assembled using the NEB Gibson assembly kit and cloned into pPK2BarGFPD digested by *SpeI/EcoRV*, forming the donor DNA sequence donor-NNT-neo.

PEG-mediated transformation of *M. thermophila* protoplasts was performed as described previously [43]. For target gene deletion, a mixture of 10 μg of PCR amplicons of the *Cas9* expression cassette, donor DNA cassette, and sgRNA cassette at a molar ratio of 1:1:1 was co-transformed into *M. thermophila* JG207 protoplasts. Putative transformants were selected with genomycin (G418), followed by sequential identification via PCR. The primer sequences used in this study are listed in Additional file 8.

Statistical significance tests and data plotting

Significant differences were analyzed by a two-tailed Student's t test with Microsoft Excel 2019. R packages including pheatmap (v1.0.8) and ggplot2 (v2.2.1) were used for data plotting.

Nomenclature

IDMS	Isotope dilution mass spectrometry
EMP	Embden–Meyerhof pathway
PPP	Pentose phosphate pathway
TCA	Tricarboxylic acid cycle
NADH	Reduced form of nicotinamide-adenine dinucleotide
NAD ⁺	Nicotinamide-adenine dinucleotide
NADPH	Reduced form of nicotinamide-adenine dinucleotide phosphate
NADP ⁺	Nicotinamide-adenine dinucleotide phosphate
ATP	Adenosine triphosphate
ADP	Adenosine diphosphate
G6P	Alpha-d-glucose 6-phosphate
F6P	Beta-d-fructose 6-phosphate
FBP	Beta-d-fructose 1,6-bisphosphate
DHAP	Dihydroxy acetone phosphate
GAP	Glyceraldehyde 3-phosphate
2PG	2-Phospho-d-glycerate
3PG	3-Phospho-d-glycerate
PEP	Phosphoenolpyruvate

PYR	Pyruvic acid
X5P	d-xylulose 5-phosphate
RL5P	d-ribulose 5-phosphate
R5P	d-ribose 5-phosphate
E4P	d-erythrose 4-phosphate
S7P	Sedoheptulose 7-phosphate
CIT	Citrate
ICIT	Isocitrate
AKG	α -Ketoglutaric acid
SUC	Succinic acid
FUM	Fumaric acid
MAL	Malic acid
Ala	Alanine
Ser	Serine
Gly	Glycine
Asp	Aspartic acid
Asn	Asparagine
Glu	Glutamic acid
Gln	Glutamine
Thr	Threonine
Val	Valine
Leu	Leucine
Ile	Isoleucine
Met	Methionine
His	Histidine
Tyr	Tyrosine
Phe	Phenylalanine
Trp	Tryptophan
Pro	Proline

Supplementary Information

The online version contains supplementary material available at <https://doi.org/10.1186/s12934-024-02570-3>.

- Supplementary Material 1: Time-profile data of the fermentation process
- Supplementary Material 2: The isotopic information of amino acids
- Supplementary Material 3: Measured and simulated MDVs of amino acids
- Supplementary Material 4: Flux distribution and minimal SSR
- Supplementary Material 5: Stoichiometric metabolic model of *Myceliophthora thermophila*
- Supplementary Material 6: Metabolomic data
- Supplementary Material 7: Supplementary information of batch fermentation validation
- Supplementary Material 8: Primers used for the genetic manipulation in this study

Acknowledgements

The authors would like to acknowledge the National Key R&D Program of China (2018YFA0900500) and Tianjin Synthetic Biotechnology Innovation Capacity Improvement Project (TSBICIP-CXRC-033).

Author contributions

JJ carried out kinetic parameter measurements, 13 C-labeled experiments, 13 C flux calculations and metabolomics analysis. DL cultivated the spores and measured the amino acid composition of the biomass. JL constructed the *M. thermophila* JG207 Δ NNT strain. CT provided malic acid high production strain *M. thermophila* JG207. YZ and JX guided the experimental design and data analysis. All authors reviewed the manuscript.

Funding

This work was financially supported by the National Key R&D Program of China (2018YFA0900500) and the Tianjin Synthetic Biotechnology Innovation Capacity Improvement Project (TSBICIP-CXRC-033 and TSBICIP-PTJJ-006).

Data availability

No datasets were generated or analysed during the current study.

Declarations

Ethics approval and consent to participate

Not applicable.

Consent for publication

All the authors agree to publish this review.

Competing interests

The authors declare no competing interests.

Received: 19 June 2024 / Accepted: 25 October 2024

Published online: 02 November 2024

References

- Goldberg I, Rokem JS, Pines O. <ArticleTitle Language="En">Organic acids: old metabolites, new themes. *J Chem Technol Biotechnol*. 2006;81:1601–11.
- Zhang X, Wang X, Shanmugam KT, Ingram LO. L-malate production by metabolically engineered *Escherichia coli*. *Appl Environ Microbiol*. 2011;77:427–34.
- Zelle RM, de Hulster E, van Winden WA, de Waard P, Dijkema C, Winkler AA, Geertman JM, van Dijken JP, Pronk JT, van Maris AJ. Malic acid production by *Saccharomyces cerevisiae*: engineering of pyruvate carboxylation, oxaloacetate reduction, and malate export. *Appl Environ Microbiol*. 2008;74:2766–77.
- Brown SH, Bashkurova L, Berka R, Chandler T, Doty T, McCall K, McCulloch M, McFarland S, Thompson S, Yaver D, Berry A. Metabolic engineering of *Aspergillus oryzae* NRRL 3488 for increased production of L-malic acid. *Appl Microbiol Biotechnol*. 2013;97:8903–12.
- Xu Y, Shan L, Zhou Y, Xie Z, Ball AS, Cao W, Liu H. Development of a Cre-loxP-based genetic system in *Aspergillus niger* ATCC1015 and its application to construction of efficient organic acid-producing cell factories. *Appl Microbiol Biotechnol*. 2019;103:8105–14.
- Li J, Lin L, Sun T, Xu J, Ji J, Liu Q, Tian C. Direct production of commodity chemicals from lignocellulose using *Myceliophthora thermophila*. *Metab Eng*. 2020;61:416–26.
- Chae TU, Choi SY, Kim JW, Ko YS, Lee SY. Recent advances in systems metabolic engineering tools and strategies. *Curr Opin Biotechnol*. 2017;47:67–82.
- Choi KR, Jang WD, Yang D, Cho JS, Park D, Lee SY. Systems Metabolic Engineering Strategies: Integrating Systems and Synthetic Biology with Metabolic Engineering. *Trends Biotechnol*. 2019;37:817–37.
- Sauer U. Metabolic networks in motion: 13 C-based flux analysis. *Mol Syst Biol*. 2006;2:62.
- Long CP, Antoniewicz MR. Metabolic flux analysis of *Escherichia coli* knockouts: lessons from the Keio collection and future outlook. *Curr Opin Biotechnol*. 2014;28:127–33.
- d'Espaux L, Ghosh A, Runguphan W, Wehrs M, Xu F, Konzock O, Dev I, Nhan M, Gin J, Reider Apel A, et al. Engineering high-level production of fatty alcohols by *Saccharomyces cerevisiae* from lignocellulosic feedstocks. *Metab Eng*. 2017;42:115–25.
- Junker BH. Flux analysis in plant metabolic networks: increasing throughput and coverage. *Curr Opin Biotechnol*. 2014;26:183–8.
- Hiller K, Metallo CM. Profiling metabolic networks to study cancer metabolism. *Curr Opin Biotechnol*. 2013;24:60–8.
- Liu Q, Ying SH, Li JG, Tian CG, Feng MG. Insight into the transcriptional regulation of *Msn2* required for conidiation, multi-stress responses and virulence of two entomopathogenic fungi. *Fungal Genet Biol*. 2013;54:42–51.
- Liu Q, Gao RR, Li JG, Lin LC, Zhao JQ, Sun WL, Tian CG. Development of a genome-editing CRISPR/Cas9 system in thermophilic fungal species and its application to hyper-cellulase production strain engineering. *Biotechnol Biofuels* 2017;10:1.
- Feist AM, Palsson BO. The biomass objective function. *Curr Opin Microbiol*. 2010;13:344–9.
- Ye R, Huang M, Lu H, Qian J, Lin W, Chu J, Zhuang Y, Zhang S. Comprehensive reconstruction and evaluation of *Pichia pastoris* genome-scale metabolic model that accounts for 1243 ORFs. *Bioresour Bioprocess*. 2017;4:22.
- Zamboni N, Fendt SM, Ruhl M, Sauer U. (13)C-based metabolic flux analysis. *Nat Protoc*. 2009;4:878–92.

19. San Román M, Cancela H, Acerenza L. Source and regulation of flux variability in *Escherichia coli*. *BMC Syst Biol*. 2014;8:1–11.
20. Freilich S, Kreimer A, Borenstein E, Gophna U, Sharan R, Ruppin E. Decoupling Environment-Dependent and Independent Genetic Robustness across Bacterial Species. *PLoS Comput Biol*. 2010;6:e1000690.
21. Heyland J, Fu J, Blank LM, Schmid A. Carbon metabolism limits recombinant protein production in *Pichia pastoris*. *Biotechnol Bioeng*. 2011;108:1942–53.
22. Takama M, Nosoh Y. Effect of ATP on glucose-6-phosphate isomerase from *Bacillus caldotenax*. *Biochim Biophys Acta*. 1982;705:127–30.
23. Blank LM, Lehmebeck F, Sauer U. Metabolic-flux and network analysis in fourteen hemiascomycetous yeasts. *FEMS Yeast Res*. 2005;5:545–58.
24. Toya Y, Hirasawa T, Morimoto T, Masuda K, Kageyama Y, Ozaki K, Ogasawara N, Shimizu H. 13 C-metabolic flux analysis in heterologous cellulase production by *Bacillus subtilis* genome-reduced strain. *J Biotechnol*. 2014;179:42–9.
25. Yao R, Li J, Feng L, Zhang X, Hu H. (13)C metabolic flux analysis-guided metabolic engineering of *Escherichia coli* for improved acetol production from glycerol. *Biotechnol Biofuels*. 2019;12:29.
26. Qi H, Li S, Zhao S, Huang D, Xia M, Wen J. Model-driven redox pathway manipulation for improved isobutanol production in *Bacillus subtilis* complemented with experimental validation and metabolic profiling analysis. *PLoS ONE*. 2014;9:e93815.
27. Wu Y, Chu W, Yang J, Xu Y, Shen Q, Yang H, Xu F, Liu Y, Lu P, Jiang K, Zhao H. Metabolic Engineering of *Enterobacter aerogenes* for Improved 2,3-Butanediol Production by Manipulating NADH Levels and Overexpressing the Small RNA RyhB. *Front Microbiol*. 2021;12:754306.
28. Hatefi Y, Yamaguchi M. Nicotinamide nucleotide transhydrogenase: A model for utilization of substrate binding energy for proton translocation. *Faseb J*. 1996;10:444–52.
29. Gu SY, Wu TJ, Zhao JQ, Sun T, Zhao Z, Zhang L, Li JE, Tian CG. Rewiring metabolic flux to simultaneously improve malate production and eliminate by-product succinate accumulation by *Myceliophthora thermophila*. *Microb Biotechnol* 2024;17:2.
30. Crown SB, Ahn WS, Antoniewicz MR. Rational design of (1)(3)C-labeling experiments for metabolic flux analysis in mammalian cells. *BMC Syst Biol*. 2012;6:43.
31. Crown SB, Antoniewicz MR. Parallel labeling experiments and metabolic flux analysis: Past, present and future methodologies. *Metab Eng*. 2013;16:21–32.
32. Douma RD, de Jonge LP, Jonker CT, Seifar RM, Heijnen JJ, van Gulik WM. Intracellular metabolite determination in the presence of extracellular abundance: Application to the penicillin biosynthesis pathway in *Penicillium chrysogenum*. *Biotechnol Bioeng*. 2010;107:105–15.
33. de Jonge LP, Douma RD, Heijnen JJ, van Gulik WM. Optimization of cold methanol quenching for quantitative metabolomics of *Penicillium chrysogenum*. *Metabolomics*. 2012;8:727–35.
34. Lu H, Liu X, Huang M, Xia J, Chu J, Zhuang Y, Zhang S, Noorman H. Integrated isotope-assisted metabolomics and (13)C metabolic flux analysis reveals metabolic flux redistribution for high glucoamylase production by *Aspergillus niger*. *Microb Cell Fact*. 2015;14:147.
35. Thienpont LM, Van Uytendange K, Blincko S, Ramsay CS, Xie H, Doss RC, Keevil BG, Owen LJ, Rockwood AL, Kushnir MM, et al. State-of-the-art of serum testosterone measurement by isotope dilution-liquid chromatography-tandem mass spectrometry. *Clin Chem*. 2008;54:1290–7.
36. Carnicer M, Baumann K, Topfitz I, Sanchez-Ferrando F, Mattanovich D, Ferrer P, Albiol J. Macromolecular and elemental composition analysis and extracellular metabolite balances of *Pichia pastoris* growing at different oxygen levels. *Microb Cell Fact*. 2009;8:65.
37. Young JD. INCA: a computational platform for isotopically non-stationary metabolic flux analysis. *Bioinformatics*. 2014;30:1333–5.
38. Antoniewicz MR, Kelleher JK, Stephanopoulos G. Elementary metabolite units (EMU): a novel framework for modeling isotopic distributions. *Metab Eng*. 2007;9:68–86.
39. Liu D, Xu Z, Li J, Liu Q, Yuan Q, Guo Y, Ma H, Tian C. Reconstruction and analysis of genome-scale metabolic model for thermophilic fungus *Myceliophthora thermophila*. *Biotechnol Bioeng*. 2022;119:1926–37.
40. Antoniewicz MR, Kelleher JK, Stephanopoulos G. Determination of confidence intervals of metabolic fluxes estimated from stable isotope measurements. *Metab Eng*. 2006;8:324–37.
41. Liu Q, Gao R, Li J, Lin L, Zhao J, Sun W, Tian C. Development of a genome-editing CRISPR/Cas9 system in thermophilic fungal *Myceliophthora* species and its application to hyper-cellulase production strain engineering. *Biotechnol Biofuels*. 2017;10:1.
42. Xie S, Shen B, Zhang C, Huang X, Zhang Y. sgRNACas9: a software package for designing CRISPR sgRNA and evaluating potential off-target cleavage sites. *PLoS ONE*. 2014;9:e100448.
43. Yang F, Gong Y, Liu G, Zhao S, Wang J. Enhancing cellulase production in thermophilic fungus *Myceliophthora thermophila* ATCC42464 by RNA interference of cre1 gene expression. *J Microbiol Biotechnol*. 2015;25:1101–7.

Publisher's note

Springer Nature remains neutral with regard to jurisdictional claims in published maps and institutional affiliations.